

**IN FLIGHT CALIBRATION OF THE PSF
FOR THE PN CAMERA.**

EPIC-MCT-TN-012 Simona Ghizzardi

27 June, 2002

Contents

1	The data set and the method	2
2	Results	4
2.1	The core radius and the slope as a function of the energy and of the off-axis angle	4
2.2	2-D fit for the King core radius and the slope as functions of energy and off-axis angle	10
2.3	Reliability of final output model.	14
2.4	Encircled Energy Fraction	16

1 The data set and the method

In this document, I report the results of the calibration of the on-axis and off-axis PSF using in orbit data concerning the PN camera.

The data set includes 110 observations taken both in the commissioning phase and in the calibration and performance verification phase. Data include observations performed in different operating modes (Full Frame, Double Node, Large Window, Small Window) with different filters. The off-axis angles of the observed sources range from 0.21 to 9.55 arcmin but most of them are nearly on-axis, within $\lesssim 2$ arcmin.

In order to study the dependence on energy of the PSF, we divided the whole spectral range [0-12 keV] in different intervals: [200-400], [400-800], [800-1200], [1200-2400], [2400-5000], [5000-8000], [8000-12000] eV, corresponding to mean energies 0.3, 0.6, 1, 1.8, 3.7, 6.5, 10 keV.

All the observations have been filtered in order to have “cleaned” event lists, where bright/dark pixels/columns have been removed and the events associated to the soft protons have been discarded. For all the runs, only monopixels have been considered.

In order to build the radially averaged profile of each source of the sample for each selected energy range, the same procedures used for the MOS PSF calibration have been adopted. The method and the algorithms have been extensively described in the report concerning the MOS calibration: <http://xmm.vilspa.esa.es/docs/documents/CAL-TN-0022-1-0.ps.gz>. All the analysis procedures are developed in IDL language.

In order to make a direct comparison with the MOS results, we built the images and the radial profiles of the PN PSF using a pixel size of $1.1''$. Such pixel size is smaller than the PN physical one, being the PN pixel $4.1''$ wide. Correspondingly, the PSF radial profiles are expected to be flat in the inner 3-4 bins. The “physical macropixels” are clearly visible in the images (see Fig. 1 as an example) built with a *binsize* = $1.1''$.

Before analyzing in detail the results, we can immediately outline some differences with respect the MOS case.

- Unlike the MOS, the PN pixel size is not much smaller than the expected width of the PSF. Correspondingly, the determination of the core radius is quite tricky.
- A substantial difference between the MOS and the PN cameras is the importance of the pile-up effect. In spite of the larger pixel size, which should enhance the effect of pile-up, the frame time for the PN is much shorter with respect to the MOS one. This induces a strong reduction of the pile-up in PN observations with respect to MOS. In addition, the large pixel size produces a spread of the events on the

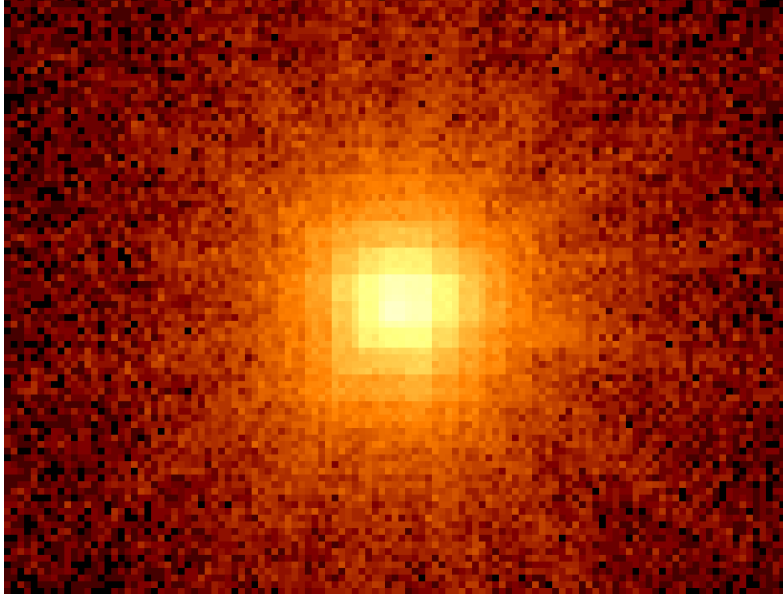


Figure 1: A PSF image with pixel size of 1.1 arcsec. The larger (4.1 arcsec) physical pixels can be recognized in the image.

whole central pixels. As a consequence, the pile-up effect is strongly reduced in PN measurements and in no cases do we observe the central holes present in the MOS strongly piled-up profiles.

- The determination of the centroid is more uncertain in the PN analysis. This is due to the PN large pixel size and it is particularly true for the Small Window mode, where, if the source is not centered in the window (as in the most of cases) only few tens of pixels can be used to find the centroid.
- Lastly, the PN has a quite large effective area. Correspondingly the data have in general a very good statistics, providing a good determination of the best fit parameters.

Following the results coming from MOS PSF calibration, we used a *King + bkg* function

$$PSF = A \left\{ \frac{1}{\left[1 + \left(\frac{r}{r_c} \right)^2 \right]^\alpha} + bkg \right\}. \quad (1)$$

to represent the radially averaged PSF profile. The *bkg* constant describes the background.

The core radius r_c and the slope α are functions of the energy and of the off-axis angle.

2 Results

By using the procedures adopted for the MOS PSF calibration, two sets (r_c and α) of best fit parameters corresponding to different selected energies and off-axis angles have been derived.

Before describing the results, we briefly outline the expected behavior of both these shape parameters with the energy and the off-axis angle. The core radius is expected to decrease when the energy increases, because the photons with higher energy will be reflected and focused only by the inner shells of the X-ray telescope. The reduced number of involved shells diminishes the source of “dispersion”; furthermore, the inner shells are probably less irregular. Both these effects improve the ability of focusing by the telescope with increasing energy. Unlike the core, which becomes smaller when moving towards higher energies, the wings should become broader as energy increases. This is expected as high energy photons have a wavelength nearer to the roughness size of the telescope shells than low energy photons, with an enhanced probability of scattering processes. This effect gives prominence to the wings of the PSF, which become, for higher energies, more important. Consequently, the slope parameter α should decrease with increasing energy. When moving off-axis, in general, the shape of the PSF will be distorted. Nevertheless, in this analysis we consider radially averaged profiles and the distortions are neglected. Moreover, for large off-axis angles, the telescope will lose ability of focusing and the PSF will be broadened; correspondingly the slope should decrease for increasing off-axis angles.

In the following paragraph (§2.1), I will analyze the behavior of the core radius and of the slope versus energy and off-axis angle, separately. In §2.2, instead, r_c and α are considered as 2-d functions of both energy and off-axis angles and the analytical modelization of these parameters will be provided. In §2.3, I will discuss the reliability of the final output model and I will define the *range of application*, i.e., those energies and off-axis angles for which the model can be applied. In §2.4, the Encircled Energy Fraction is studied.

2.1 The core radius and the slope as a function of the energy and of the off-axis angle

In this paragraph we study the core radius and the slope as functions of the energy and of the off-axis angle separately, when the other variable is fixed.

In Fig. 2, I plotted some examples of core radius (left column) and of the slope (right column) versus energy, at three different off-axis angles. The core radius is in arcsec and the energy is in keV. Off-axis angles are in arcmin.

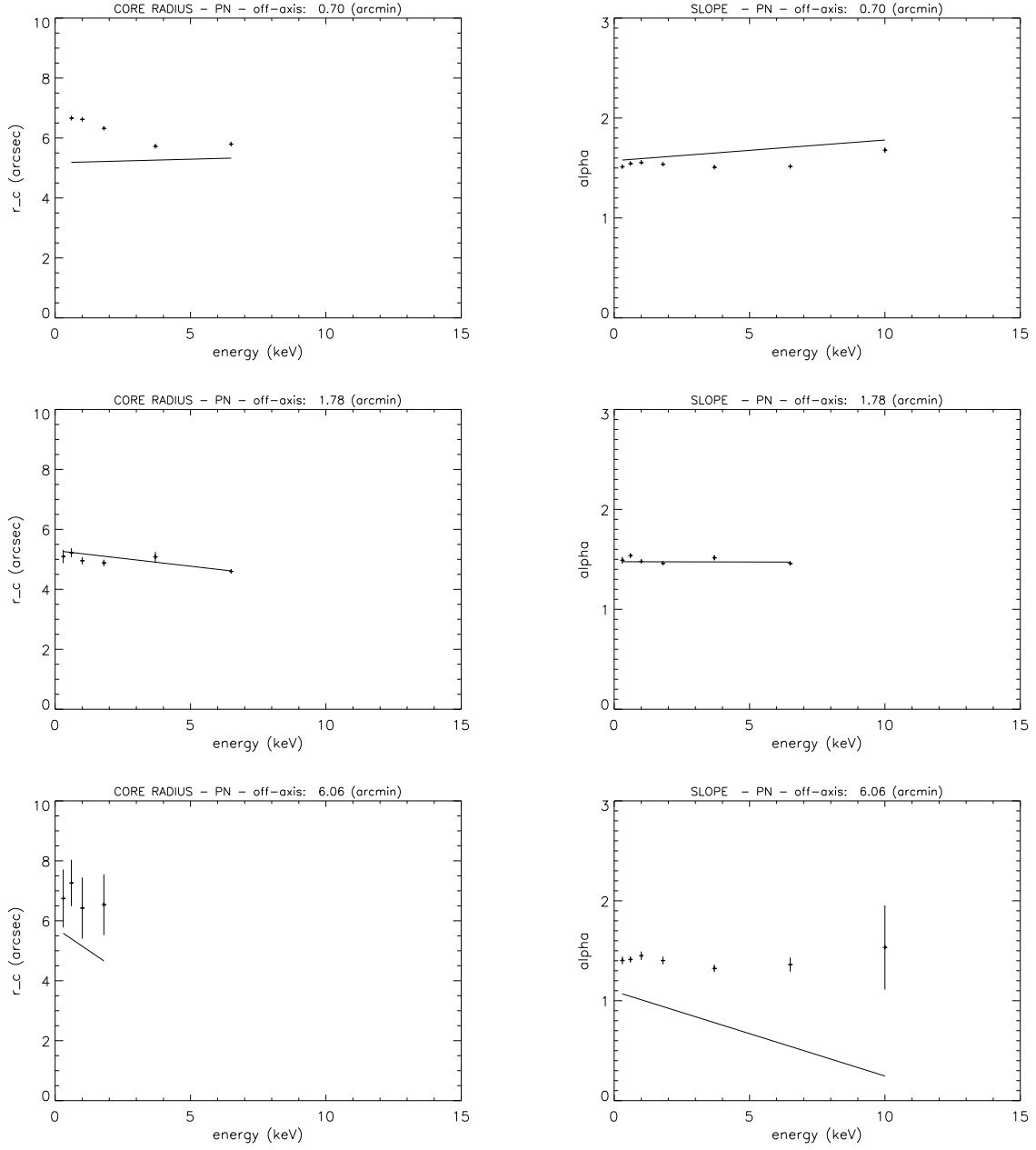


Figure 2: King core radius (left column) and King slope (right column) vs. energy (keV) for some off-axis angles. The solid lines refer to the 2-d fit (see §2.2).

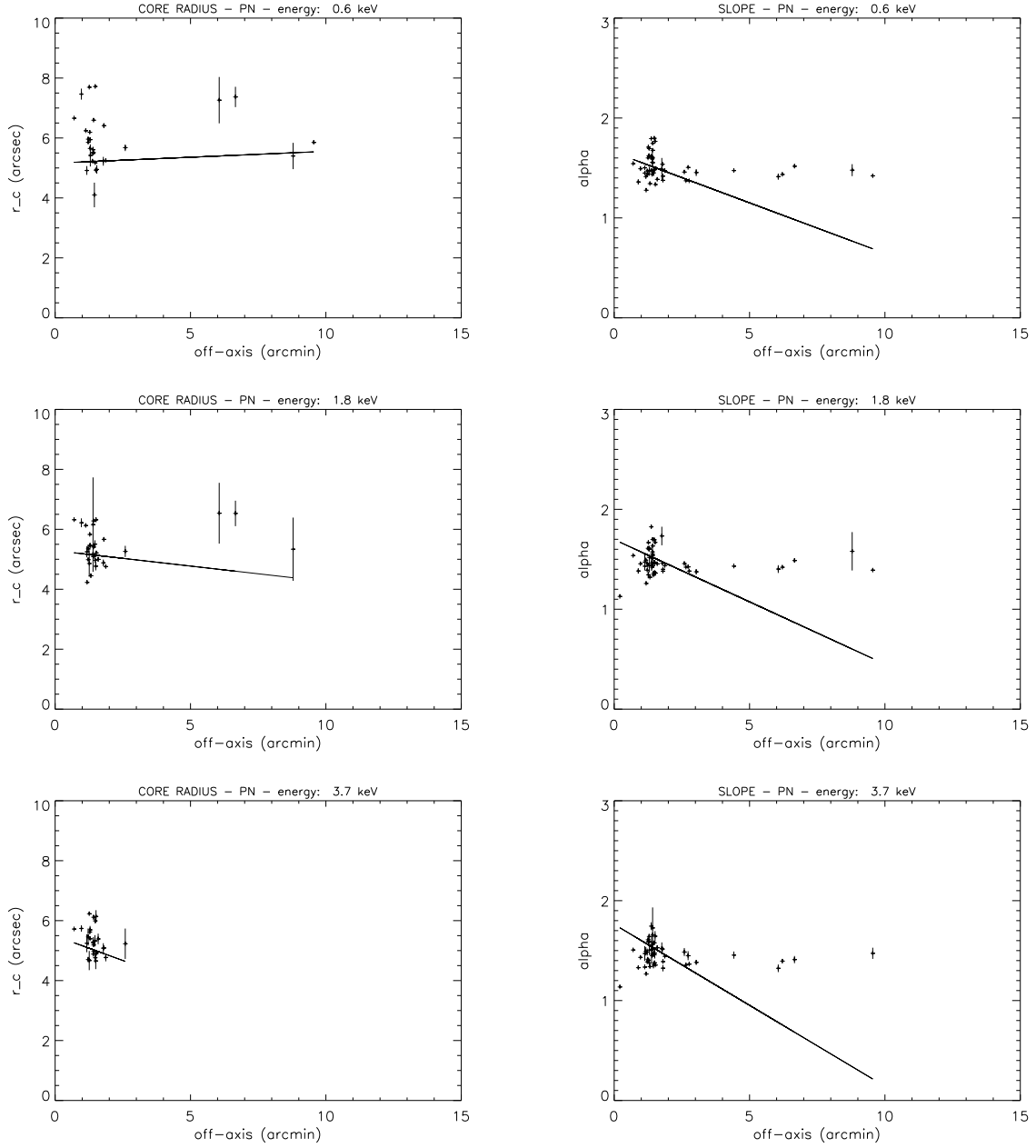


Figure 3: King core radius (left column) and King slope (right column) vs. off-axis angle (arcmin) for 0.6, 1.8 and 3.7 keV. The solid lines refer to the 2-d fit (see §2.2).

As expected, the core tends to decrease as energy increases. Similarly to the MOS, when moving towards large off-axis angles, the number of points available is smaller, but in any case the trend holds. The behavior of the slope is analogous to the MOS one, with very small variations for increasing energy. The lines overplotted in the graphs *are not* the best fit, but the result of the 2-d fit which will be discussed in §2.2.

The best fit line does not match the data when considering large off-axis angles. This point is even more evident if we plot the core radius and the slope as functions of the off-axis angle at each fixed energy. In Fig. 3, I plotted, for the energies 0.6, 1.8, 3.7 keV, the core radius (in arcsec) and the slope in the left column and in the right column respectively versus the off-axis angle (in arcmin). Again, the 2-d fit is not able to represent adequately the data points. In particular, this holds for large off-axis angles.

In both Fig. 2 and 3, we can observe that data are rather scattered and most of them are in nearly on-axis positions, with off-axis angles within ~ 2 arcmin. Hence, the 2-d fit is completely driven by the large quantity of scattered data at small off-axis angles, leading to unreliable values when considering points off-axis or points at high energies.

In order to find a reliable fit, a possible way out consists in binning data. We bin the off-axis angle variable, using bins $12''$ wide. Figs. 4 and 5 show the new binned points for off-axis angle and for energy fixed. The solid lines are again the results of the 2-d fit. The scatter is largely reduced especially for the α parameter and the best 2-fit lines match the data points.

We can see that the core shows a decreasing trend with the off-axis angle and with energy. When considering larger energies, the large off-axis angles are no longer sampled and, as will be discussed in §2.3 for these energies, the modelization must be restricted only to the nearly on-axis positions, where the trend seems similar to the low energies one. Similarly to the MOS results, the slope doesn't show any significant variation with the off-axis angle.

Before concluding this paragraph, some comments about the possible reasons of the large scatter observed in Figs. 2 and 3 are needed. Actually, it is not easy to understand what induces such a large scatter. It could be simply related to different sources which could have slightly different profiles. However, sometimes, the same source observed at the same conditions (off-axis angle) shows clearly different behaviors. As an example we plot in Fig. 6 the radial profiles of two observations of LMC X-3 at $1.13'$ off-axis angle. Apart from some differences in the behavior of the core, (the Full Frame observation could be weakly affected of some pile-up) the two slopes have a quite different steepness. This is one of the cases contributing to the scatter of nearly on-axis points in Figs. 2 and 3. There are several possibilities which can explain the origin of this scatter. First of all, it is

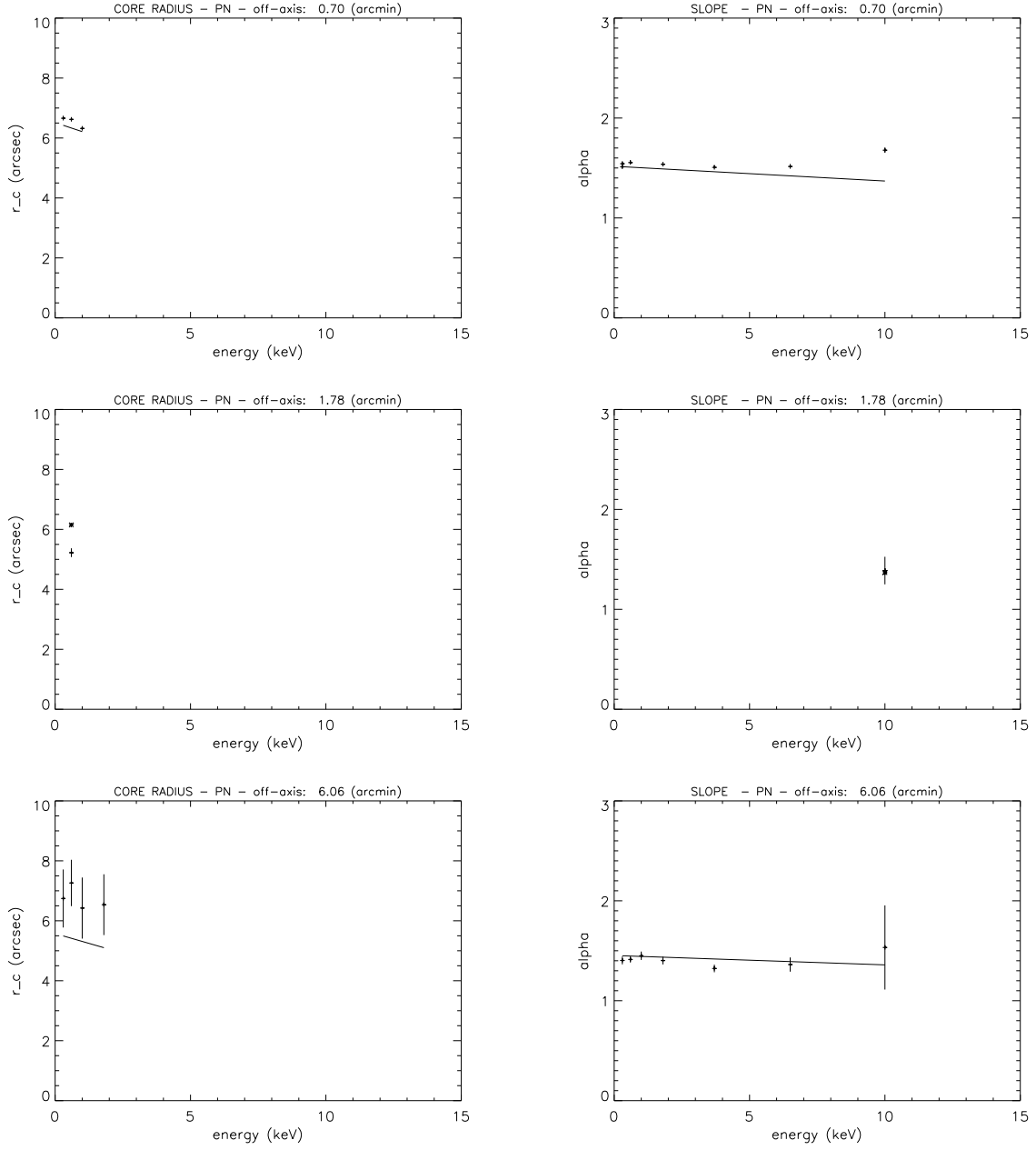


Figure 4: King core radius (left column) and King slope (right column) vs. energy (keV) for some off-axis angles with binned points. The solid lines refer to the 2-d fit (see §2.2).

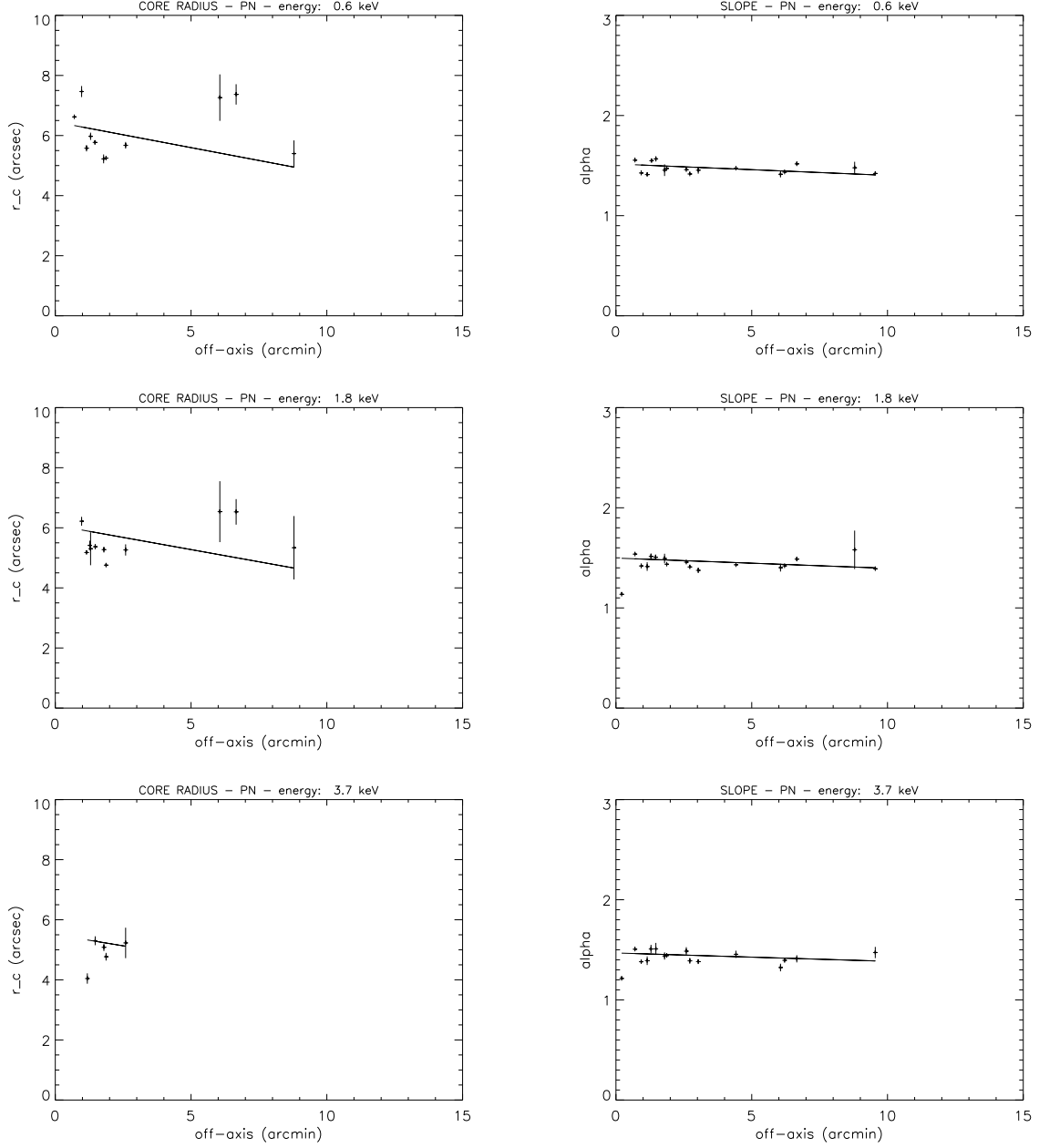


Figure 5: King core radius (left column) and King slope (right column) vs. off-axis angle (arcmin) for 0.6, 1.8 and 3.7 keV with binned points. The solid lines refer to the 2-d fit (see §2.2).

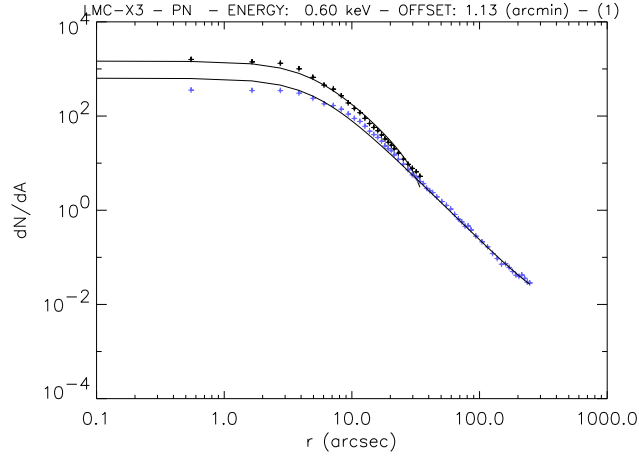


Figure 6: Radial profiles for two observation of LMC X-3 at 1.13' off-axis angle.

worth to notice that we do not correct for out of time events which can be important, and which have different weight in different operative modes. Moreover, the pile-up could be underestimated because of the spreading of the events in the central pixel. Lastly, as we will discuss later on, the determination of the centroid can play a crucial role, especially in Small Window measurements.

2.2 2-D fit for the King core radius and the slope as functions of energy and off-axis angle

The two shape parameters r_c and α can be studied as 2-d functions of energy and off-axis angle and can be written according to:

$$r_c(E, \Theta) = a + b \cdot E + c \cdot \Theta + d \cdot E \cdot \Theta, \quad (2)$$

and

$$\alpha(E, \Theta) = x + y \cdot E + z \cdot \Theta + w \cdot E \cdot \Theta. \quad (3)$$

The fit has been performed considering the energy E in keV units and the off-axis angle Θ in arcmin units; r_c is in arcsec. The coefficients a and x give the order of magnitude of r_c and α respectively. The other coefficients give the variations with energy and off-axis positions.

In Figs. 7 and 8 we draw the 2-d best fit for r_c and α in a 3-d plot and in a contour plot.

The values obtained by fitting the available sets of r_c and α with eqs. (2) and (3) are

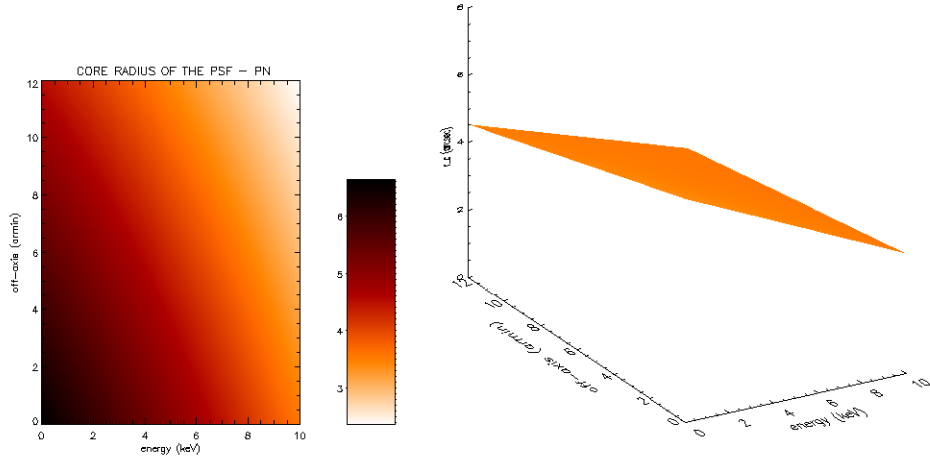


Figure 7: King core radius as a function of the off-axis angle and energy.

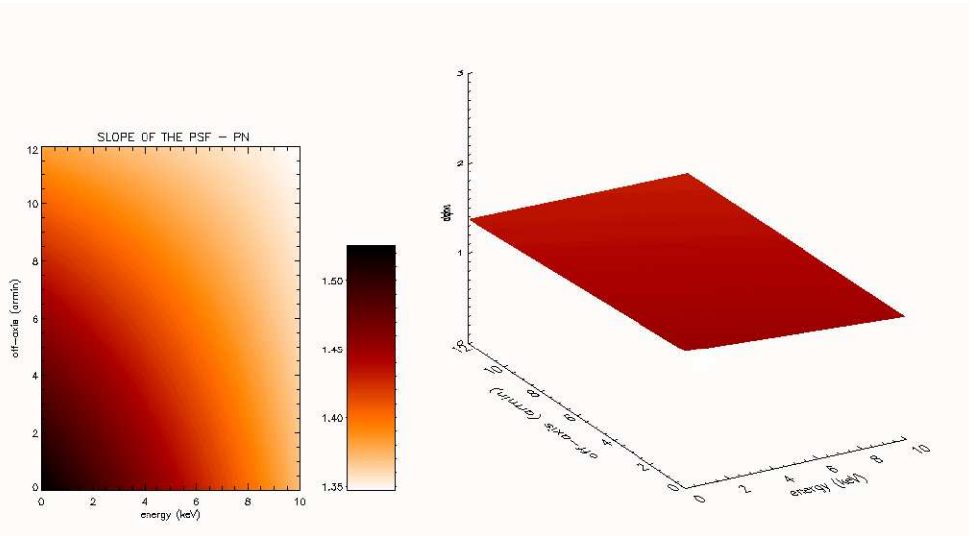


Figure 8: King slope as a function of the off-axis angle and energy.

Table 1: r_c and α best fit according to eqns. (2) and (3). For comparison we reported also the results of the two MOS cameras.

	PN			
r_c	$a = 6.636 \pm 0.020$	$b = -0.305 \pm 0.032$	$c = -0.175 \pm 0.010$	$d = -0.0067 \pm 0.0185$
α	$x = 1.525 \pm 0.001$	$y = -0.015 \pm 0.001$	$z = -0.012 \pm 0.001$	$w = -0.0010 \pm 0.0004$
	MOS 1			
r_c	$a = 5.074 \pm 0.001$	$b = -0.236 \pm 0.001$	$c = 0.002 \pm 0.001$	$d = -0.0180 \pm 0.0006$
α	$x = 1.472 \pm 0.003$	$y = -0.010 \pm 0.001$	$z = -0.001 \pm 0.002$	$w = -0.0016 \pm 0.0013$
	MOS 2			
r_c	$a = 4.759 \pm 0.018$	$b = -0.203 \pm 0.010$	$c = 0.014 \pm 0.017$	$d = -0.0229 \pm 0.0133$
α	$x = 1.411 \pm 0.001$	$y = -0.005 \pm 0.001$	$z = -0.001 \pm 0.002$	$w = -0.0002 \pm 0.0011$

reported in Table 1. For comparison, we reported also the best fitting values for the two MOS cameras.

In Table 2, we report also some values for the core and the slope for the on-axis position at three different energies. Again the corresponding values for the MOS cameras are reported for comparison.

From both Tables 1 and 2, it is evident that the PN PSF is slightly worst with respect both the two MOS cameras, because of a larger core radius.

In Fig. 9, we plot some radial profiles with the best fit curves. The best fit profiles are obtained by constraining the core and the slope to the 2-d best fit values reported in Tables 1 and 2. We can observe that, in general, the fit lines match quite well the data. In the panel in Fig. 9 corresponding to PKS0558, we can see that the Small Window profile is distorted in the core and in fact, the best fit line does not reproduce fairly the data, whereas the same profile is suitable in describing the other two curves. This is related to the fact that the determination of the centroid is quite difficult, especially in the Small Window mode, as pointed out previously. In the case of PKS0558, the simultaneous fit is crucial to find reliable values for r_c and α . The same is not possible in all cases, e.g. when there is only the Small Window measure. For 3C273 in Small Window (see panel at top-right of Fig. 9), we can see that the final best fit line does not match very well the data in the core region. The core region actually is badly determined because of a bad centroiding. This problem surely contributes to produce the scatter in the data

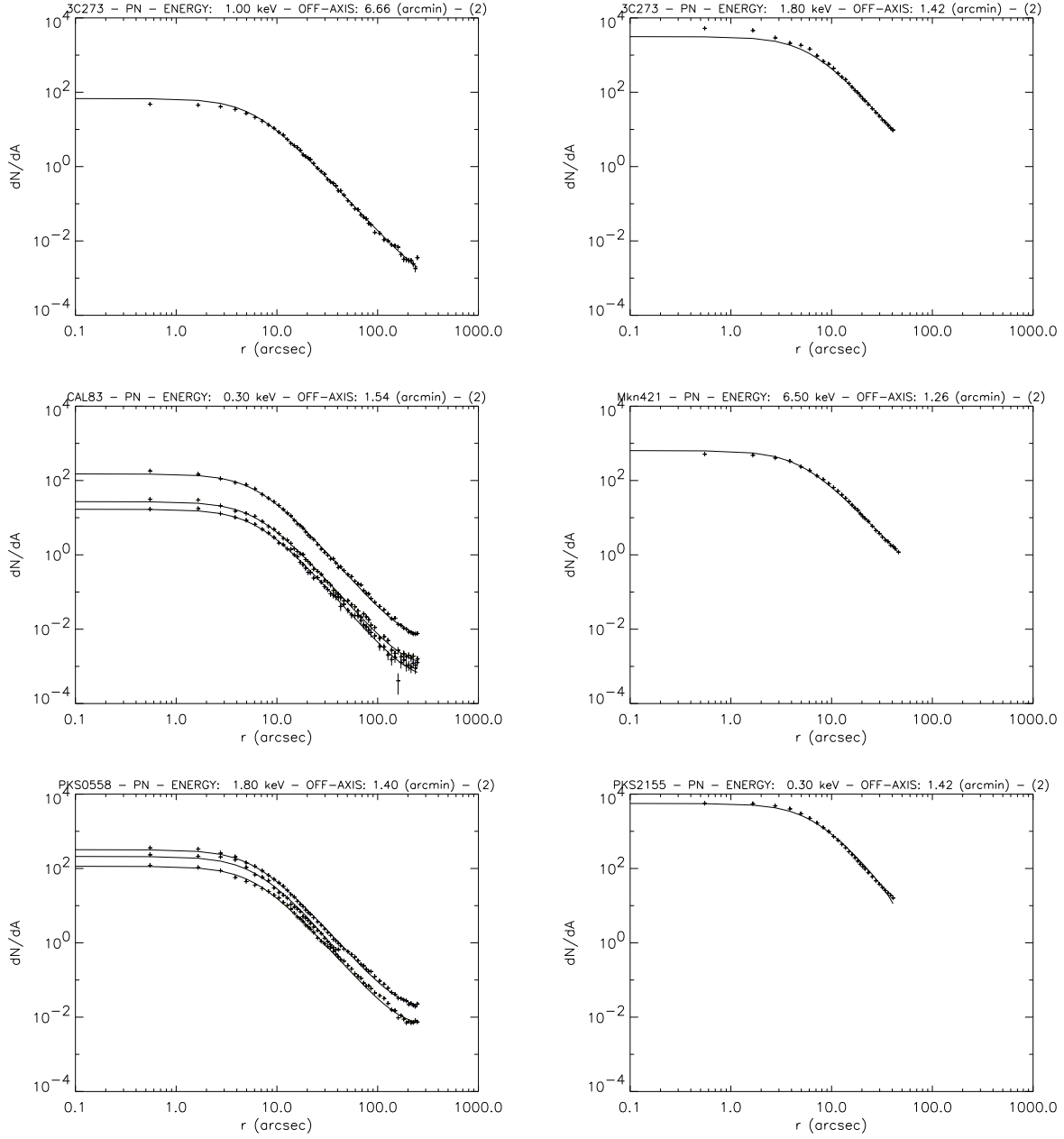


Figure 9: Some radial profiles at different energies and off-axis angles. The solid lines correspond to the best fit with r_c and α fixed to the values obtained through eqs. (2) and (3) and values in Table 1

Table 2: r_c and α best fit values for 1.5, 8, 9 keV. For comparison we reported also the results of the two MOS cameras.

PN					
r_c			α		
1.5 keV	8 keV	9 keV	1.5 keV	8 keV	9 keV
6.18''	4.18''	3.88''	1.50	1.40	1.39
MOS 1					
r_c			α		
1.5 keV	8 keV	9 keV	1.5 keV	8 keV	9 keV
4.72''	3.18''	2.95''	1.46	1.39	1.38
MOS 2					
r_c			α		
1.5 keV	8 keV	9 keV	1.5 keV	8 keV	9 keV
4.45''	3.13''	2.93''	1.40	1.37	1.36

distribution described previously.

2.3 Reliability of final output model.

Similarly to the MOS case, data tend to disappear when moving towards high energies and large off-axis angles. As a matter of fact, no informations are available there, hence **the calibration for these regions is not available**.

In Figs. 10 and 11, I replotted Figs. 7 and 8 with the sample data points marked on. While the slope is well sample almost in all the plane energy-off-axis angle, the core radius limits the regions where the model can be used.

Correspondingly, the eqns. (2) and (3) with values listed in Table 1 are valid only within regions covered by asterisks in the figures. The regions covered by the asterisks define the **range of application** of the model, and as a matter of fact, it is defined by the regions where the core radius is available. So, the high energy and high off-axis angle region is excluded from the *range of application*. The model cannot be used there.

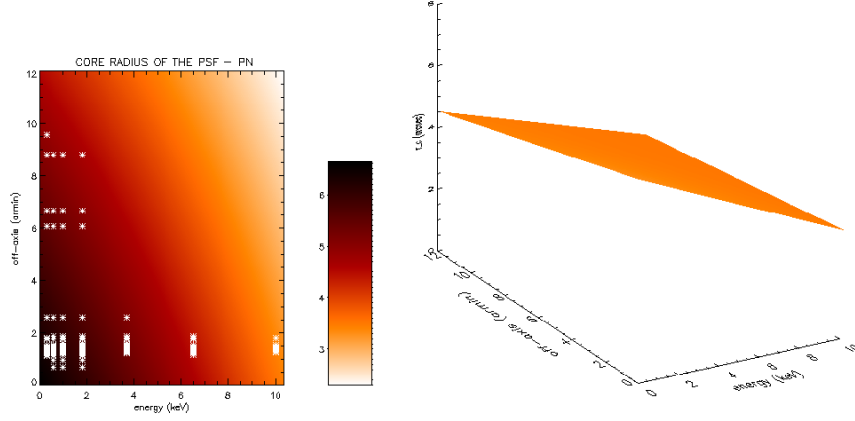


Figure 10: King core radius as a function of the off-axis angle and energy. Superimposed crosses correspond to measured data points.

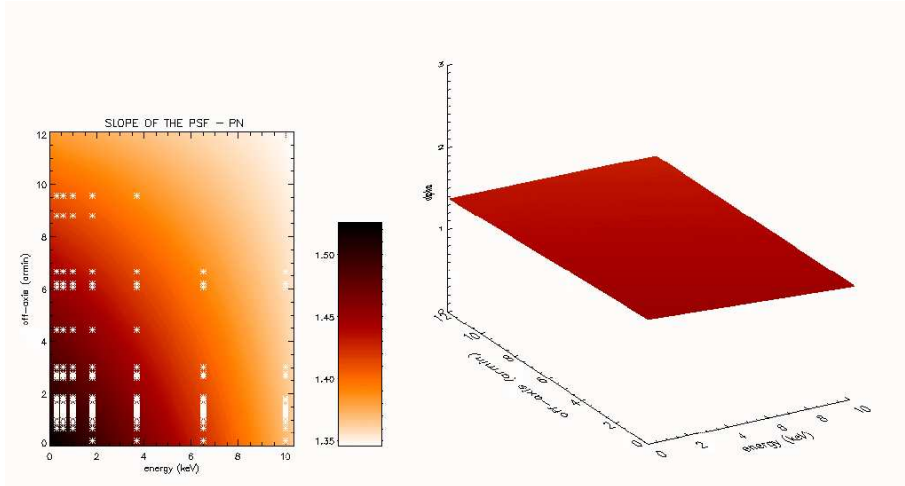


Figure 11: King slope as a function of the off-axis angle and energy. Superimposed crosses correspond to measured data points.

Similarly to what we did for the MOS, we divide the space energy–off-axis angles in three regions. The region where data are available and reliable is marked with green and the calibration model can be used there. The inferred parameters can not be used in the red region corresponding to the energies and off-axis angles where data are absent. For the MOS cameras, also a yellow region corresponding to data with very large errors was present. In this region, the model should be used with caution. However, this region is not present for PN. For PN in fact, statistics is very good. Hence, where data are present, error bars are quite small and the results are reliable. In the PN reliability plot, only the red and the green regions are present.

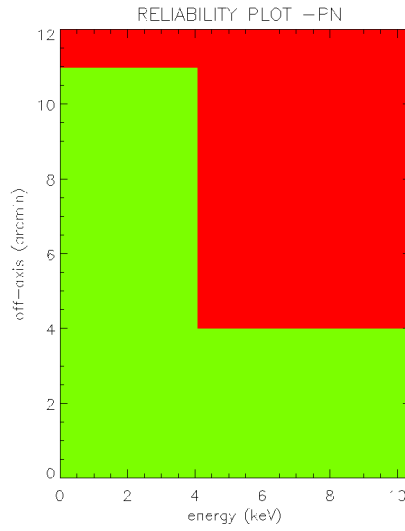


Figure 12: Plot showing the reliability of the modelization of the PSF. The red region marks the points for which calibration measures are not available and correspondingly there is no calibration. The green region corresponds to those energies and off-axis angles for which the calibration is well-sampled and the modelization provides a good description of the PSF.

2.4 Encircled Energy Fraction

The Encircled Energy Fraction, which specifies the fraction f of energy collected within a certain radius R is defined according to:

$$EEF(R) = \frac{\int_0^R PSF(r) r dr}{\int_0^{R_N} PSF(r) r dr}. \quad (4)$$

For the King profile:

$$EEF(R) = \frac{1 - \frac{1}{\left[1 + \left(\frac{R}{r_c}\right)^2\right]^{\alpha-1}}}{1 - \frac{1}{\left[1 + \left(\frac{R_N}{r_c}\right)^2\right]^{\alpha-1}}} = f. \quad (5)$$

As for the MOS calibration, we fixed $R_N = 5$ arcmin. The radius R enclosing a fraction f of energy is:

$$R(f; r_c, \alpha) = r_c \left\{ \left[1 - f \left(1 - \frac{1}{\left[1 + \left(\frac{R}{r_c}\right)^2\right]^{\alpha-1}} \right) \right]^{\frac{1}{1-\alpha}} - 1 \right\}^{\frac{1}{2}}. \quad (6)$$

In Figs. 13 and 14, we show the radii enclosing 50% and 80% of the energy. Considering that α is roughly constant with energy and off-axis angles, the main behavior of R is similar to that of r_c . Note that, as the PSF, the EEF defined in eqn. (5) is valid only within the range of application introduced in §2.3 and represented in Fig. 12.

In Figs. 15 and 16, we show the radius enclosing 50% and 80% of the total energy, for the on-axis position. The radius is plotted in arcsec unit.

In Table 3 the values of $R(50\%)$ and $R(80\%)$ are reported for the energies 1.5, 8, 9 keV, for PN and also for MOS 1 and MOS 2 for comparison.

As for the PSF, the PN EEF is slightly worst than the MOS one. The radius enclosing a fraction f of energy is always greater for the PN.

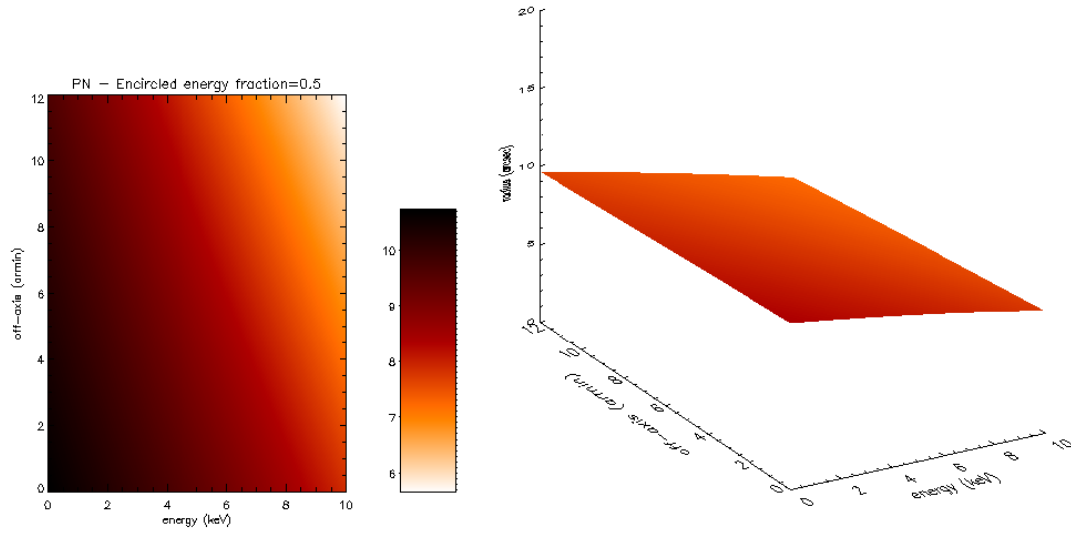


Figure 13: Radius enclosing 50% of energy (arcsec units).

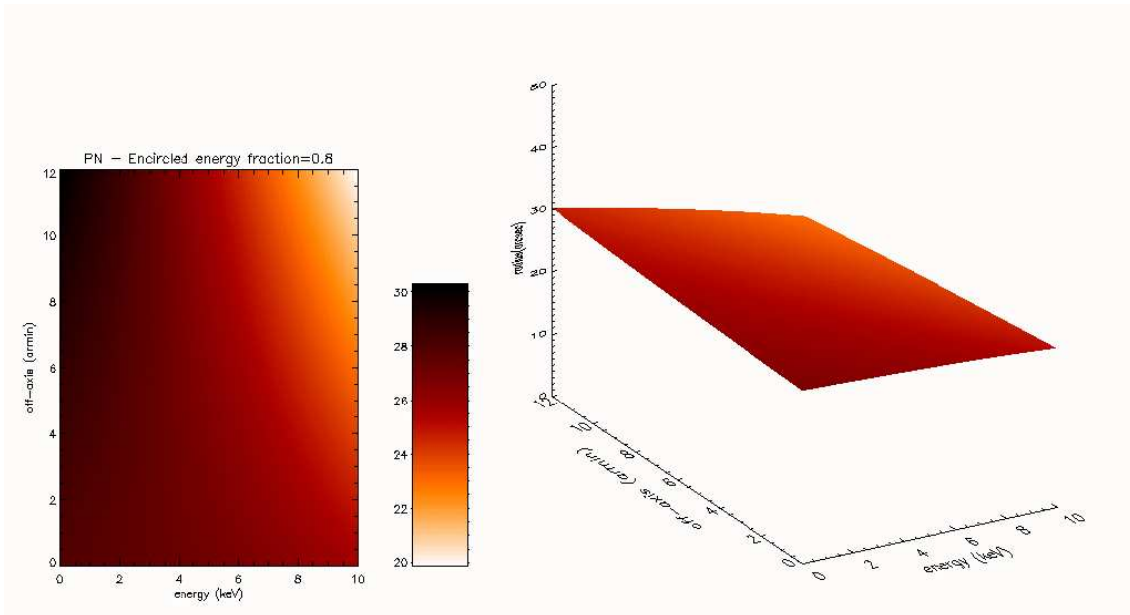


Figure 14: Radius enclosing 80% of energy (arcsec units).

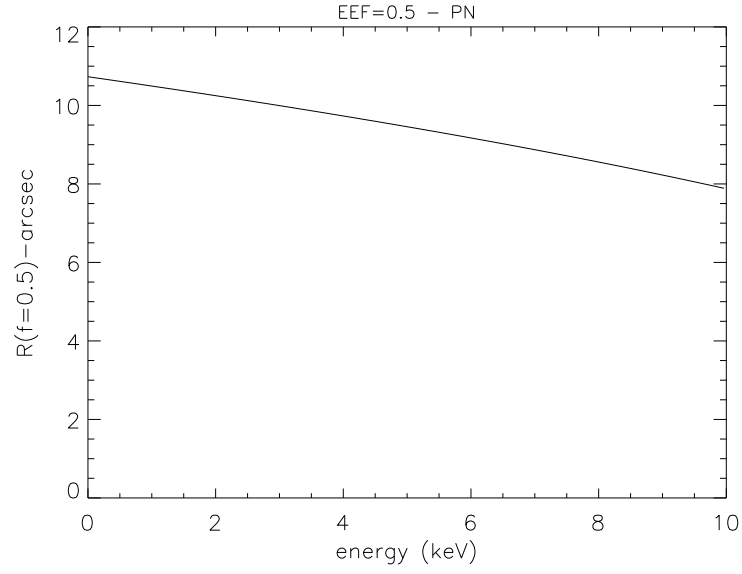


Figure 15: Radius enclosing 50% of energy (arcsec units) for the on-axis position.

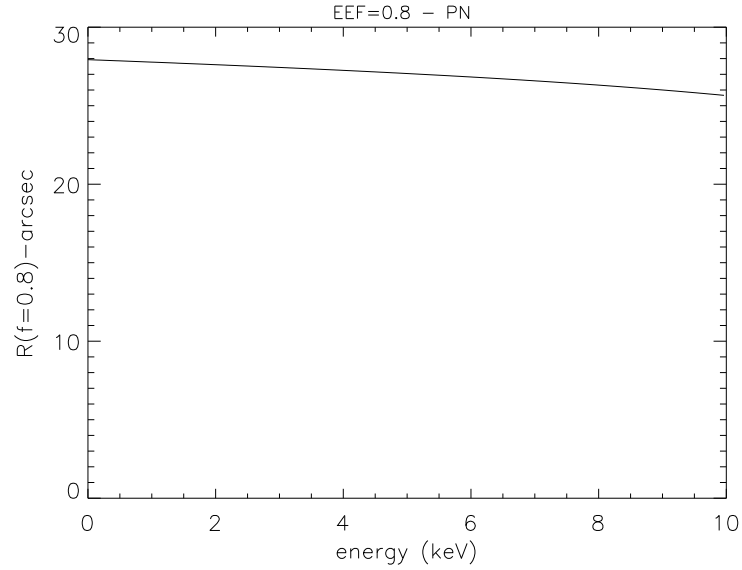


Figure 16: Radius enclosing 80% of energy (arcsec units) for the on-axis position.

Table 3: Radii enclosing 50% and 80% of the energy at the energies of 1.5, 8, 9 keV, for the on-axis PSF. For comparison also the corresponding MOS values are reported.

PN					
$R(50\%)$			$R(80\%)$		
1.5 keV	8 keV	9 keV	1.5 keV	8 keV	9 keV
10.37''	8.56''	8.23''	27.70''	26.31''	26.00''
MOS 1					
$R(50\%)$			$R(80\%)$		
1.5 keV	8 keV	9 keV	1.5 keV	8 keV	9 keV
8.6''	6.7''	6.4''	24.5''	21.5''	20.9''
MOS 2					
$R(50\%)$			$R(80\%)$		
1.5 keV	8 keV	9 keV	1.5 keV	8 keV	9 keV
9.1''	7.0''	6.6''	27.7''	23.1''	22.3''